molecules

MDPI

Article

Synthesis, X-ray Crystallography, Spectroscopic Characterizations, Density Functional Theory, and Hirshfeld Surface Analyses of a Novel (Carbonato) Picket Fence Iron(III) Complex

Mondher Dhifet [1,2], Bouzid Gassoumi [3], Maxim A. Lutoshkin [4], Anna S. Kazachenko [5], Aleksandr S. Kazachenko [4], Omar Al-Dossary [6], Noureddine Issaoui [7,8,*] and Habib Nasri [1]

1 Laboratory of Physical Chemistry of Materials (LR01ES19), Faculty of Sciences of Monastir, University of Monastir, Avenue of the Environment, Monastir 5019, Tunisia; mondherdhifet_2005@yahoo.fr (M.D.); habib.nasri@fsm.rnu.tn (H.N.)
2 Faculty of Sciences of Gafsa, University of Gafsa, Sidi Ahmed Zarrouk, Gafsa 2112, Tunisia
3 Laboratory of Advanced Materials and Interfaces (LIMA), Faculty of Science of Monastir, University of Monastir, Avenue of Environnment, Monastir 5000, Tunisia; gassoumibouzid2016@gmail.com
4 Institute of Chemistry and Chemical Technology, Krasnoyarsk Scientific Center, Siberian Branch, Russian Academy of Sciences, Akademgorodokst, 50/24, 660036 Krasnoyarsk, Russia; maximsfu@yahoo.com (M.A.L.); kaalla@list.ru (A.S.K.)
5 Institute of Non-Ferrous Metals, Siberian Federal University, pr. Svobodny, 79, 660041 Krasnoyarsk, Russia; leo_lion_leo@mail.ru
6 Department of Physics and Astronomy, College of Science, King Saud University, P.O. Box 2455, Riyadh 11451, Saudi Arabia; omar@ksu.edu.sa
7 Laboratory of Quantum and Statistical Physics LR18ES18, Faculty of Sciences of Monastir, Avenue of the Environment, Monastir 5079, Tunisia
8 Higher Institute of Computer Sciences and Mathematics of Monastir, University of Monastir, Monastir 5000, Tunisia
* Correspondence: issaoui_noureddine@yahoo.fr

check for updates

Citation: Dhifet, M.; Gassoumi, B.; Lutoshkin, M.A.; Kazachenko, A.S.; Kazachenko, A.S.; Al-Dossary, O.; Issaoui, N.; Nasri, H. Synthesis, X-ray Crystallography, Spectroscopic Characterizations, Density Functional Theory, and Hirshfeld Surface Analyses of a Novel (Carbonato) Picket Fence Iron(III) Complex. *Molecules* **2024**, *29*, 3722. https://doi.org/10.3390/molecules29163722

Academic Editor: Franck Rabilloud

Received: 13 June 2024
Revised: 24 July 2024
Accepted: 26 July 2024
Published: 6 August 2024

Copyright: © 2024 by the authors. Licensee MDPI, Basel, Switzerland. This article is an open access article distributed under the terms and conditions of the Creative Commons Attribution (CC BY) license (https://creativecommons.org/licenses/by/4.0/).

Abstract: An Fe(III)-carbonato six-coordinate picket fence porphyrin complex with the formula [K(2,2,2-crypt)][Fe^{III}(TpivPP)(CO_3)]·C_6H_5Cl·$3H_2O$ (**I**) has been synthesized and characterized by UV-Vis and FT-IR spectra. The structure of (carbonato)(α,α,α,α-tetrakis(*o*-pivalamidophenyl)porphinato) ferrate(III) was also established by XRD. The iron atom is hexa-coordinated by the four nitrogen atoms of the pyrrol rings and the two oxygen atoms of the CO_3^{2-} group. Complex **I**, characterized as a ferric high-spin complex (S = 5/2), presented higher Fe-Np (2.105(6) Å) and Fe-P_C (0.654(2) Å) distances. Both X-ray molecular structure and Hirshfeld surface analysis results show that the crystal packing of **I** is made by C-H···O and C-H···Cg weak intermolecular hydrogen interactions involving neighboring [Fe^{III}(TpivPP)(CO_3)]$^-$ ion complexes. Computational studies were carried out at DFT/B3LYP-D3/LanL2DZ to investigate the HOMO and LUMO molecular frontier orbitals and the reactivity within the studied compound. The stability of compound **I** was investigated by analyzing both intra- and inter-molecular interactions using the 2D and 3DHirshfeld surface (HS) analyses. Additionally, the frontier molecular orbital (FMO) calculations and the molecular electronic potential (MEP) analyses were conducted to determine the electron localizations, electrophilic, and nucleophilic regions, as well as charge transfer (ECT) within the studied system.

Keywords: iron(III) porphyrin; XRD; FT-IR; DFT; FMO; HS

1. Introduction

Metalloporphyrins can appear as powerful materials for the active sites of a certain number of enzymes, such as hemoproteins (hemoglobins, myoglobins, etc.) [1–4]. In the case of hemoglobin, the heme and the protein are linked together by the coordination of residues of the protein chain on the axial coordination site of iron. In general, Fe(III) can

be divided into four different electronic ground states: high-spin (S = 5/2), intermediate-spin (S = 3/2), admixed-spin (S = 5/2, 3/2), and low-spin (S = 1/2). All these situations closely resemble the properties of iron (III) hemoproteins and make iron (III) porphyrins a good model for studying and understanding several properties of biomolecules. It is noteworthy that investigations on iron (III) porphyrins with bidentate axial ligands are quite rare in the literature; for example, the carbonate is not toxic to the environment. The results obtained from the structural and spectroscopic investigation of the picket fence derivative give some idea of the relative importance of the bidentate ligand vis-à-vis the stereochemical and electronic properties of the iron(III) high-spin porphyrin species. These results provide more insight into the geometry and the electronic structure of the high-spin iron(III) porphyrin derivatives with bidentate oxyanionic ligands.

Increased equatorial Fe-Np distance results in a higher spin state of the iron(III) porphyrins. This increase in distance leads to a significant decrease in the interaction between the iron $d_{x^2-y^2}$ and porphyrin a_{2u} orbitals [5]. In general, hex-coordinated Fe(III) porphyrinates with anionic ligands can be observed in two different electronic configurations: high-spin (S = 5/2) or low-spin (S = 1/2) [6]. The five 3d orbitals of iron(III) separate into two energy groups: those of higher energy ($d_{x^2-y^2}$ and d_{z^2}) and those of lower energy (d_{xy}, d_{xz} and d_{yz}). This separation highlights the electronic spin state of the iron atom in the triflate complex, but in the [K(2,2,2-crypt)][Fe^{III}(TpivPP)(CO_3)] complex, the spin is strong (S = 5/2).

Complex **I** was characterized by both spectroscopic UV/Vis and FT-IR. The molecular structure of this new hexacoordinated iron(III) metalloporphyrin was determined by single crystal X-ray diffraction (XRD). The Hirshfeld surface examination and DFT calculations of compound **I** confirm the high-spinstate. Our study focused on the picket fence porphyrin due to its ability to stabilize ionic ligands bonded to the iron atom, making it a suitable choice for our investigation [7].

2. Results and Discussion

2.1. Experimental

2.1.1. Materials and Methods

All other solvents and reagents are used in specific cases, either to dissolve complexes or to facilitate obtaining the synthesized products. Depending on their uses, they must be treated and distilled in some cases, while in other cases, they are used commercially without any treatment.

UV/Vis spectral data for the complex were collected using WinASPECT PLUS (SPECORD PLUS version 4.2). The FT-IR spectra were carried out in the solid state on a Perkin-Elmer model 398 instrument, ranging from 4000 to 400 cm^{-1}. The crystals obtained after the diffusion of pentane in chlorobenzene were ground with dry KBr to form pellets (1–2 mg of the sample per 100 mg of KBr).

Single crystal XRD data were collected by a Bruker-Nonius FR590 Kappa CCD diffractometer. Hirshfeld surface (HS) analysis is usually performed using Crystal Explorer 3.15 [8,9]. This program generates HS and 2D fingerprint plots of a given compound using its crystallographic information file, or CIF. The "d_{norm}" Hirshfeld surface is obtained by the combination of the normalized distances from the closer atom inside the surface "d_i" and the outside of the surface "d_e" to the HS surface, showing all the intermolecular contacts of the crystal structure [10,11].

2.1.2. Preparation of [K(2,2,2-crypt)][Fe^{III}(TpivPP)(CO_3)]·C_6H_5Cl·$3H_2O$

Cryptand-222 (4,7,13,16,21,24-hexaoxa-l,l0-diazabicyclo[8.8.8]hexacosane (86.59 mg, 0.23 mmol) and potassium carbonate K_2CO_3 (55.28 mg, 0.40 mmol) were mixed together for 1 h in the chlorobenzene (V = 10 mL). [Fe^{III}(TpivPP)Cl] [12] (25 mg, 0.023 mmol) in the C_6H_5Cl (V = 5 mL) was added to the carbonato/cryptand-222 and stirred for 3 h. The hex-coordinate (carbonato)iron(III) porphyrin complex was precipitated by the addition of dry pentane.

Elemental analysis calculated for $C_{89}H_{107}ClN_{10}O_{14}FeK$ (molecular weight = 1671.285), C 63.96%, H 6.45%, N 8.38%; found: C 64.81%, H 6.11%, N 8.49%; UV/Vis: λ_{max} (nm,

chlorobenzene, logε): 424 (5.87), 576 (4.60), 607 (4.52), FT-IR (solid, cm^{-1}): 3403 (s) [ν(N-H) Pivaloyl], 2960-2871 (s), [ν(C-H) Porph.], 1680 (s) [ν(C=O) Pivaloyl], 1636 (w) [ν_1(C-O) Carbonate], 1354 [ν_2(C-O) Carbonate], 1104 (vs) [$\nu(CH_2$-O-CH_2 Cryptand-222], 988 (s) [δ(CCH) Porph.].

2.1.3. X-ray Crystallography

The crystals of the carbonato iron (III) are obtained by slow diffusion in test tubes. These crystals are washed and rinsed with pentane, then dried and well visualized on the electronic microscope while eliminating impurities. Single crystal mounted on the goniometric head using a Bruker-AXS APEX2 2014 [13]. Data were collected at room temperature using the radiation Kα of Mo (λ_{Mo} = 0.7107 Å). Complex **I** crystallizes in the monoclinic system ($P2_1/n$) with four formulas per cell (Z = 4).

The X-ray diffractionstructure was resolved using the direct method SIR-2004-1.0 [14] and refined against F^2 using the SHELXL-97 package [15]. During the refinement of the structure complex **I**, four disorder problems were encountered: (a) the *tert*-butyl group of one picket is disordered over two orientations C29A-C30A-C31A/C29B-C30B-C31B, with a major position occupancy of 0.512(7); (b) the one O atom of the TpivPP is occupying/disordered over two orientations O1A/O1B with a major position occupancy of 0.529(1); and (c) the two oxygen atoms of the CO_3^{2-} group are disordered in two positions (O5A-O6A/O5B-O6B) with a major position occupancy of 0.548(1).

The anisotropic displacement ellipsoids of complex **I** were very extended, which indicates a static disorder. For fragments involving these atoms, the ISOR/SIMU restraints [16] are used, which explains the huge number of restraints. All hydrogen atoms were placed using assumed geometry, with C-$H_{aromatic}$ = 0.95 Å and C-H_{methyl} = 0.98 Å. The displacement parameters of the H atoms were set to 1.2 (1.5 for methyl). The geometrical calculations were carried out using the program PLATON (Spek, 2002) [17]. The molecular drawings were made using ORTEP3 for Windows [18], and the packing diagrams were generated using the software MERCURY 4.0 [19].

To model the structure of compound **I**, we omitted the disordered chlorobenzene and aqua solvent molecules using the PLATON software [20]. It is obtained from our solvent-accessible voids with a volume of 4 × 229.25 $Å^3$, and the number of electrons per unit cell generated by squeeze was 4 × 22 e. The corresponding results for our compound are given in Table 1.

Table 1. Crystallographic data for complex **I**.

Empirical Formula	**$C_{83}H_{100}N_{10}O_{13}KFe$**
Formula weight, M	1649.2
T (K)	293 (2)
Wavelength(Å)	0.71073
Crystal system	monoclinic
Space group	
$P2_1/n$	
Lattice constants	
a (Å); *b* (Å); *c* (Å)	17.932 (2); 21.484 (2); 22.924 (2)
β (°)	100.813 (3)
Volume *V* ($Å^3$)	8674.8 (14)
Z	4
D_{cal}, g/cm^3	1.263
Absorption coefficient, μ (mm^{-1})	0.319
F(000)	3484
Crystal size (mm^3)	0.30 × 0.15 × 0.10

Table 1. *Cont.*

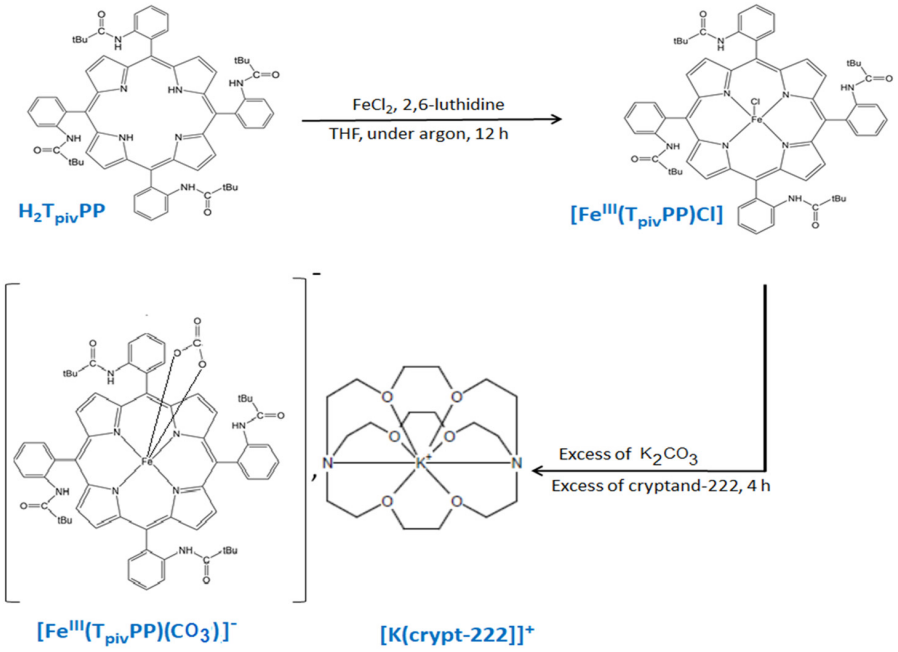
Empirical Formula	**$C_{83}H_{100}N_{10}O_{13}KFe$**
θ-range for data collection	1.6–19.8
Limiting indices	$-17 \leq h \leq 17$, $-20 \leq k \leq 20$, $-21 \leq l \leq 21$
Reflexions collected/unique	82,787/7805
R(int)/R(σ)	0.1122/0.0478
Data/Restraints/Parameters	7805/17/1028
X (Flack parameter)	0.18(2)
Final *R* indices [$I > 2\sigma(I)$]	[a] R_1= 0.083, wR_2= 0.200
R indices (all data)	R_1 = 0.103, wR_2 = 0.213
Goodness-of-fit on F_o^2	1.047
Highest peak and deepest hole (eÅ^{-3})	1.905 and −0.787
CCDC	2,367,771

[a] $R_1 = \sum | |F_o| - |F_c| | / \sum |F_o|$.

2.2. Synthesis of Complex I

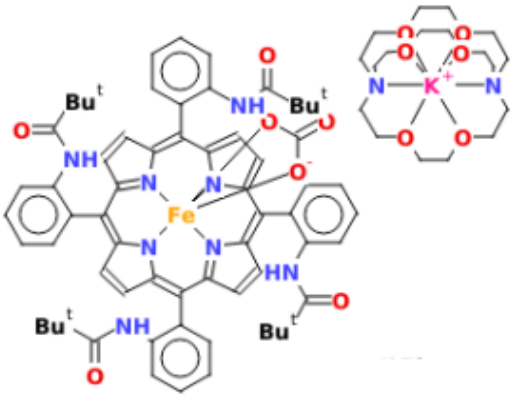
The synthesis of picket fence porphyrin was made according to the reported method [12]. The formula of this species is 4α-H_2TpivPP, but it is usually written as H_2TpivPP. Scheme S1 illustrates the different steps leading to the preparation of this *meso*-arylporphyrin, which is known to protect iron (II) porphyrins with small axial ligands that are unstable using "non-protected" porphyrin such as H_2TPP (*meso*-tetraphenylporphyrin) or H_2OEP (octaethylporphyrin). This is the case of the [Fe^{II}(TpivPP)(l-MeIm)O_2] [12] (1-MeIm = 1-methylimidazole) complex, where the oxo group is located inside the pocket of the TpivPPporphyrinate, leading to the stability of this species.

The preparation of Fe(III)-chlorido with the formula [Fe^{III}(TpivPP)Cl] was prepared according to the reported procedures [12]. In Scheme 1, the synthetic procedure of [K(2,2,2-crypt)][Fe^{III}(TpivPP)(CO_3)]·C_6H_5Cl·3H_2O, namely the (carbonato) [α,α,α,α-tetrakis(*o*-pivalamidophenyl)porphyrinato]iron(III) chlorobenzene trihydrate, is shown. Furthermore, in the formula of **I**, we omitted the disordered chlorobenzene and aqua solvent molecules using the squeeze procedure of PLATON [20], so that the formula is [K(2,2,2-crypt)][Fe^{III}(TpivPP)(CO_3)] (**I**).



Scheme 1. Scheme of the preparation of [Fe^{III}(TpivPP)Cl] [12] and complex **I**.

In Scheme 2, the chemical graph of complex **I** is shown.



Scheme 2. Two-dimensional chemical graph of complex **I**.

2.3. Spectroscopic Characterizations

The UV-visible spectra of H_2TpivlPP, [Fe^{III}(TpivPP)Cl], and complex **I** are illustrated in Figure 1. Table S1 compares the λ_{max} values with those of other *meso*-porphyrin-iron metalloporphyrin compounds.

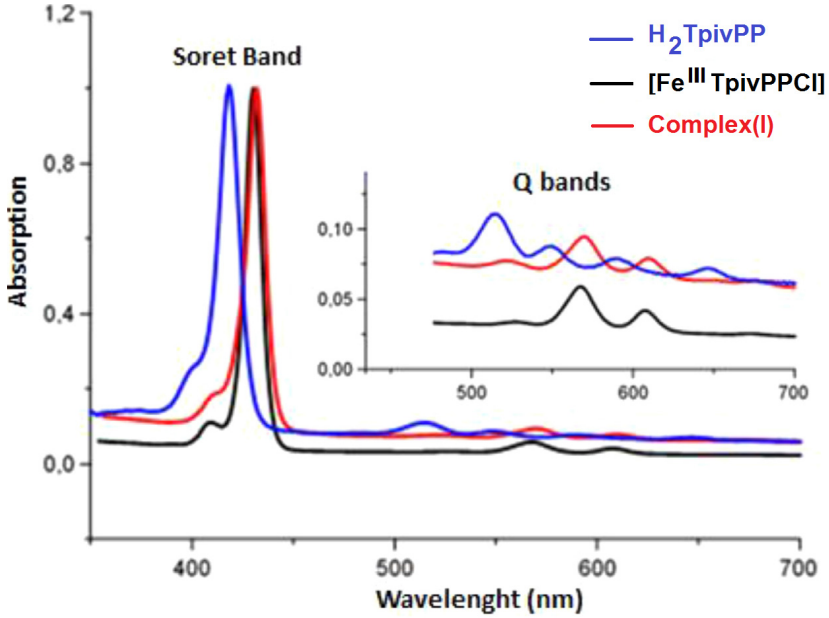


Figure 1. Electronic spectra of H_2TpivPP, [Fe(TpivPP)Cl], and complex **I** in C_6H_5Cl solution.

The concentration used for the spectrum in the Soret band region is 1.5 × 10^{-6} M, while the concentration used in the Q band area is 6.1 × 10^{-5} M. This spectrum presents a Soret band around 424 nm and a β and α bands around 576 nm and 607 nm, respectively.

These results are similar for iron(III) *meso*-porphyrin complexes with anionic axial ligands [21].

The optical gap ($E_{g\text{-}opt}$) value of complex **I** was determined using the tangent method according to the formula:

$$E_{g\text{-}opt} = 1239.8/\lambda_{Lim}$$

where λ_{Lim} is the intersection between the tangent to the highest Q band and the horizontal (Figure S1). This experimental value is 1.907 eV, which is common for porphyrins and metalloporphyrins and indicates the semi-conductor character of our carbonato iron(III) complex.

Complex **I** shows an intensive absorption peak in the infrared spectrum located at 1104 cm^{-1}, which corresponds to the -CH_2-O-CH_2- group of $[K(crypt\text{-}222)]^+$ (see Figure 2).

It exhibits typical absorption bands of H_2TpivPP with the ν(C=O) of the carbonyl group of the pivaloyl and δ(CCH) bending frequencies at 1680 cm^{-1} and 988 cm^{-1}, respectively. In the same IR spectrum of complex **I**, two weak bands at 1636 and 1356 cm^{-1} attributed to the ν_1(C-O) and ν_2(C-O) vibrations confirm the existence of the $(CO_3)^{2-}$ ligand.

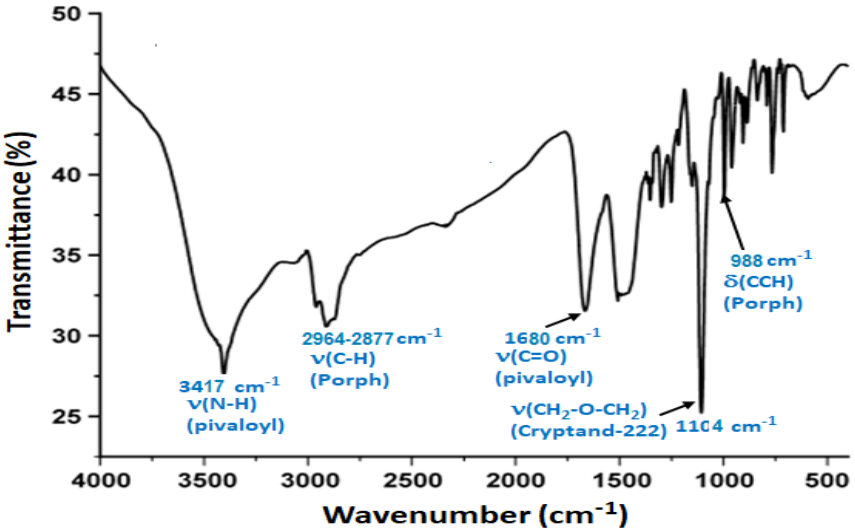


Figure 2. Experimental IR spectrum of complex **I.**

*2.4. Structural Properties of [K(2,2,2-crypt)][Fe^{III}(TpivPP)(CO_3)] (**I**)*

The asymmetric unit of (**I**) contains the anioncomplex $[Fe^{III}(TpivPP)(CO_3)]^-$ with one $[K(2,2,2\text{-crypt})]^+$ cation, one C_6H_5Cl solvent, and three molecules of water. A disordered chlorobenzene and three molecules of water, which could not be modeled, were removed from the lattice of **I** by using the squeeze procedure [20]. The ortep diagram shows the structure of the anioncomplex (see Figure 3). The geometric parameters (bond length (Å) and angles (°)) of complex **I** are reported in Table 2.

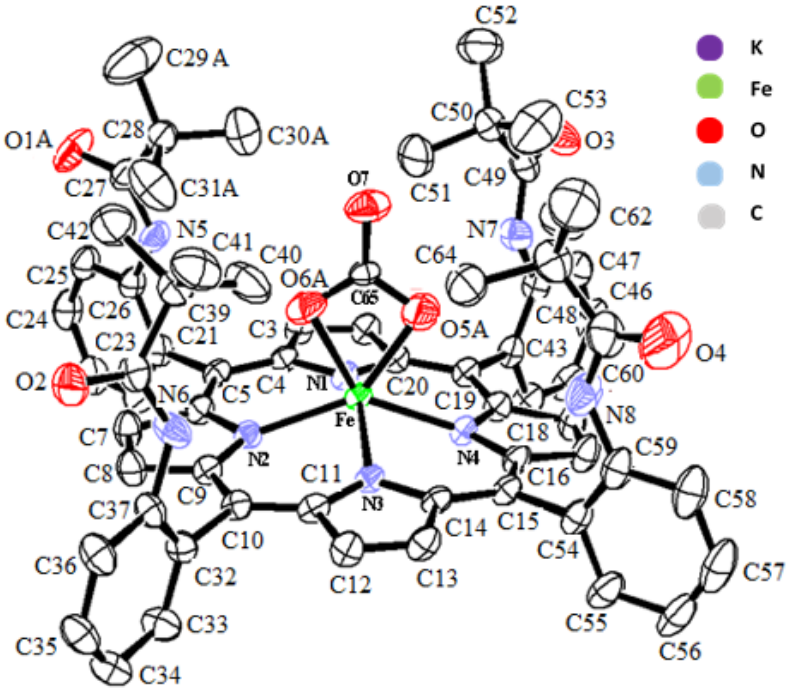


Figure 3. Ortep diagram showing the $[Fe^{III}(TpivPP)(CO_3)]^-$ ion complex. Thermal ellipsoids are drawn at the 30% probability level. Only the major positions of the disordered fragments are shown, and the hydrogen atoms have been omitted for clarity.

Table 2. Geometric parameters (distances (Å) and angles (°)) in compound **I**.

Iron Coordination Polyhedron			
Fe-N1	2.115 (6)	N1-Fe-N2	85.9 (2)
Fe-N2	2.083 (5)	N1-Fe-N3	146.7 (2)
Fe-N3	2.120 (6)	N1-Fe-N4	85.0 (2)
Fe-N4	2.101 (6)	N2-Fe-N3	85.4 (2)
Fe-N_p	2.105 (6)	N2-Fe-N4	146.9 (2)
Fe-O5A	2.00 (2)	N1-Fe-O5A	110.0 (6)
Fe-O6A	2.047 (2)	N2-Fe-O5A	136.4 (6)
N3-Fe-O5A	98.3 (6)	N3-Fe-O6A	133.8 (6)
N4-Fe-O5A	76.4 (5)	N4-Fe-O6A	118.4 (7)
N1-Fe-O6A	78.3 (6)	N2-Fe-O6A	90.6 (6)
Carbonato ligand			
C65-O5A	1.250 (2)	Fe-O6A-C65	91.9 (2)
C65-O6A	1.257 (2)	O5A-C65-O6A	99.1 (2)
C65-O7	1.292 (1)	O5A-C65-O7	132.8 (2)
Fe-O5A-C65	95.5 (1)	O6A-C65-O7	118.6 (2)
Potassium-cryptand-222			
K-N9	3.023 (7)	N9-K-N10	179.48 (2)
K-N10	3.055 (6)	N9-K-O8	59.94 (2)
K-O8	2.807 (6)	N9-K-O9	119.91 (2)
K-O9	2.839 (5)	O8-K-O9	60.15 (2)
K-O10	2.842 (2)	O8-K-O10	128.13 (2)
K-O11	2.823 (5)	O8-K-O11	100.93 (2)
K-O12	2.834 (6)	O9-K-O12	121.18 (2)
K-O13	2.767 (6)	O11-K-O12	96.55 (2)

The $[K(crypt\text{-}222)]^+$ counterion is shown in Figure S2. The K-O (crypt-222) and K-N (crypt-222) distances [2.818 (6) Å and 3.039 (6) Å, respectively] are in agreement with the literature values [21].

The geometric parameters Fe-Np, Fe-X_L, and Fe-P_C in compound **I** and a selection of some other six-coordinate iron(III) high-spin (S = 5/2) and low-spin (S = 1/2) porphyrin complexes are given in Table 3.

Table 3. Selected structural features of several hex-coordinate (porphyrinato) iron(III) derivatives.

Complex	**Fe–N_p** [a]	**Fe–X_L** [b]	**Fe–P_C** [c]	**Ref.**
High-spin (S = 5/2) iron(III) hexacoordinated metalloporphyrins				
$[Fe^{III}(TpivPP)(CO_3)]^-$	2.105	2.047 2.000	0.654(2)	T.w.
$[Fe^{III}(TpivPP)(\eta^2\text{-}O_2CO)]^-$	2.125	2.005 2.031	0.749(7)	[22]
$[Fe^{III}(TPP)(\eta^2\text{-}O_2NO)]$ [d]	2.073	2.323 2.019	0.600(1)	[23]
$[Fe^{III}(TPP)(\gamma^2\text{-}O_2NO)]$	2.085	2.124 2.268	0.620(1)	[23]
$[Fe^{III}(TTP)(OTeF_5)(THF)]$ [e]	2.053	2.334 1.967	0.200	[24]
Low-spin (S = 1/2) iron(III) hexacoordinated metalloporphyrins				
$[Fe^{III}(TpivPP)(NO_2)_2]^-$	1.992	1.985 1.985	0.020	[25]
$[Fe^{III}(TpivPP)(SC_6HF_4)(NO_2)]^-$	1.980	2.277 1.990	0.050(1)	[25]
$[Fe^{III}(TPP)(SC_6HF_4)_2]^-$	1.998	2.312 2.312	0 [f]	[26]

[a] Fe-Np: Equatorial Fe-$N_{pyrrole}$ distance. [b] Fe-X_L: Fe-axial ligand distance. [c] Fe-Pc: Fe-median plan of core distance. [d] TPP: Tetraphenylporphyrin. [e] $OTeF_5$: Teflate. [f] Value of 0 required by symmetry. T.w.: This work.

In complex **I**, Fe-Np (2.105(6) Å) and Fe-P_C (0.654(2) Å) distances are in the normal range of 2.048–2.125 Å and 0.20–0.75 Å, respectively. This value confirms clearly that compound **I** is a hexacoordinated metalloporphyrin with highspin (S = 5/2). However, six-coordinate iron (III) low-spin porphyrin species present lower Fe-P_C and Fe-Np distances. Figure 4 illustrates the crystal packing of complex **I** perpendicular to the a axis.

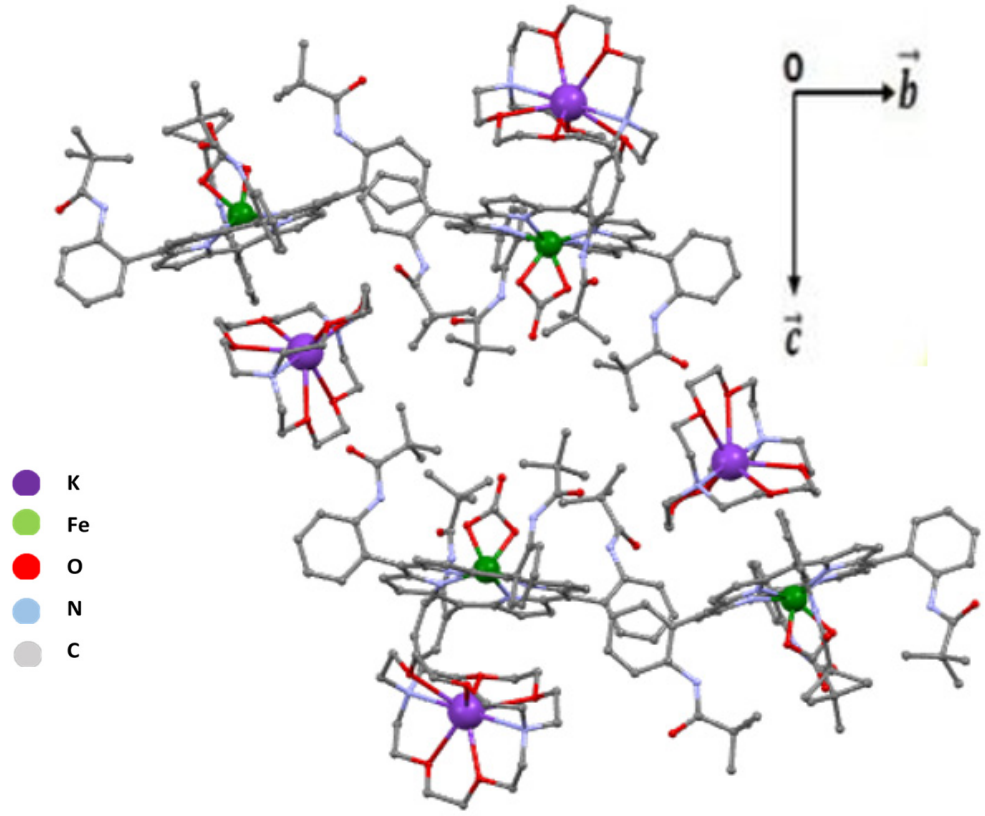


Figure 4. Projection of the packing diagram of complex **I** down the a axis. Only the major positions of the disordered fragments are shown, and the hydrogen atoms have been omitted for clarity.

In order to investigate the intermolecular interactions within the crystal packing of complex **I**, we used the PLATON program [17], as described just above, to obtain a good visualization of these intermolecular interactions (see Figures 5 and 6).

Figure 7 represents the coordination polyhedral and the environment of iron. The distances between the two O atoms O5A/O6A of the CO_3^{2-} and the iron atom are 2.047(15) Å and 2.00(2) Å, respectively. The two values of bond length are almost equal and are slightly shorter than the third distance Fe-O7 (CO_3^{2-}) bond length. The long bond length observed in our case is probably due to the type and environment of the porphyrin used.

The porphyrin core is shown in Figure 8. The Fe-porphyrin and the number of coordinations for iron have several properties for the irregular and non-planar conformation of the porphyrin core. The diagram highlights significant saddling and moderate doming distortions of the macrocycle [27].

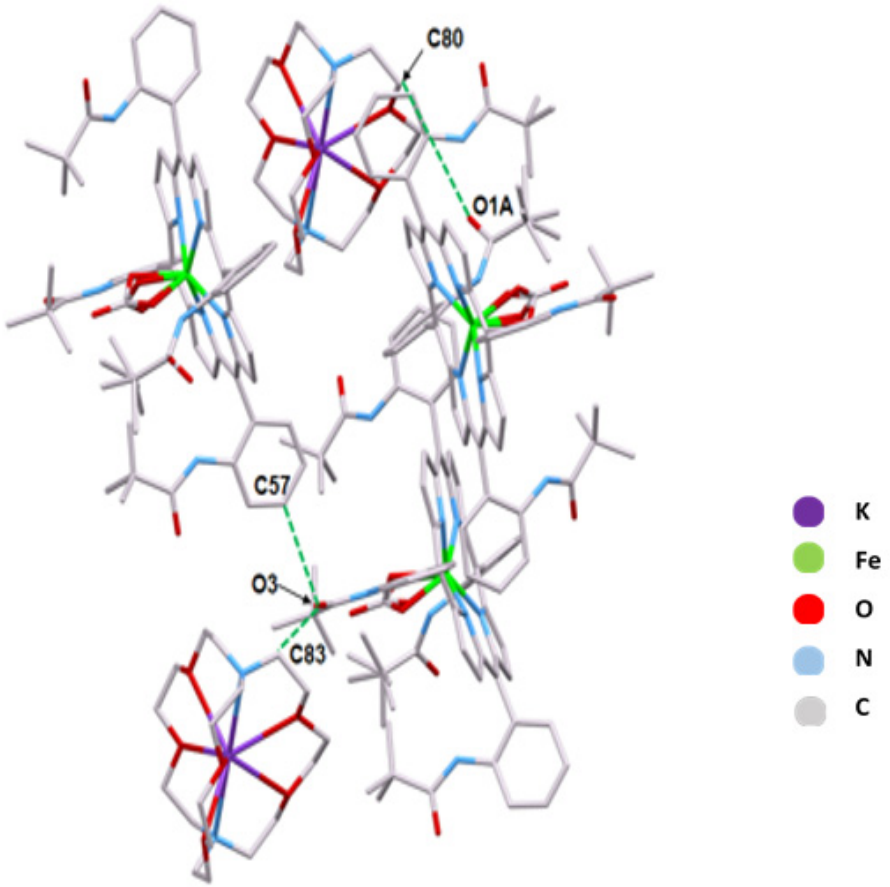


Figure 5. Drawing illustrating the C–H· · · O intermolecular interactions in complex **I**.

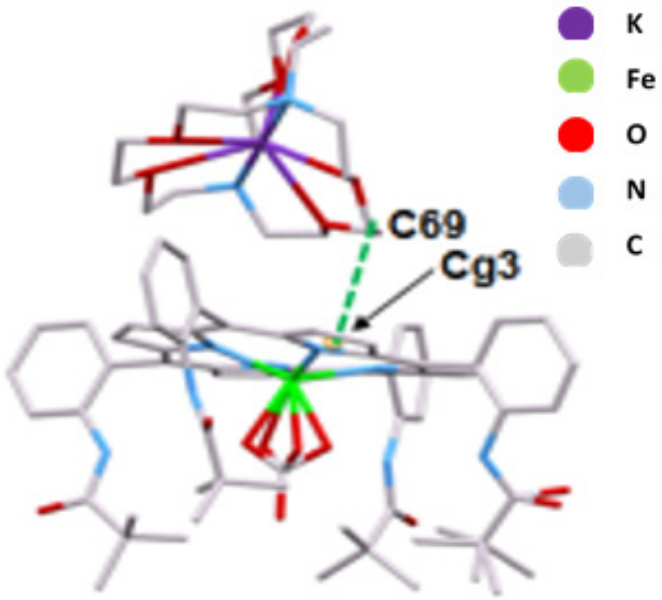


Figure 6. Drawing illustrating the C69–H69A· · · Cg3 intermolecular interactions in complex **I**.

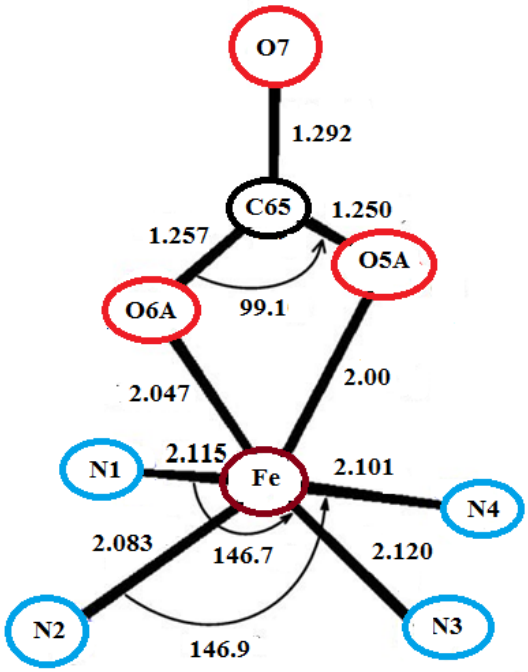


Figure 7. Geometric parameters (distances (Å)/angles (°)) of the iron coordination polyhedron.

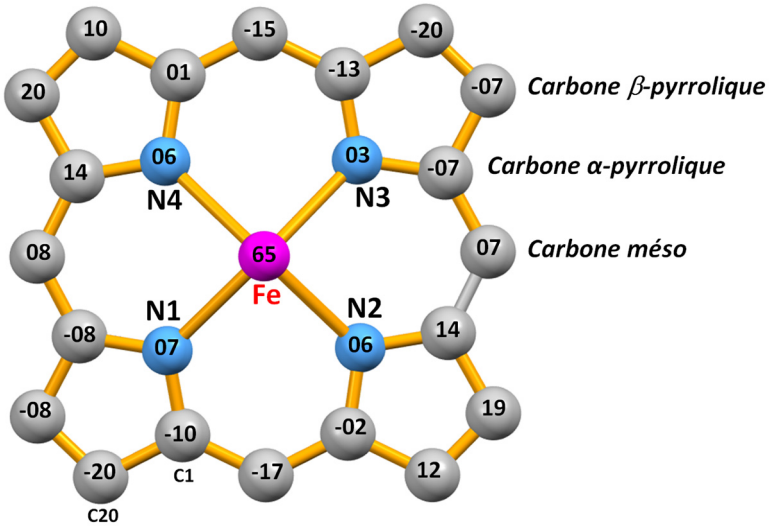


Figure 8. Porphyrin core in the $[Fe^{III}(TpivPP)(CO_3)]^-$ illustrating the displacements of each atomin units of 0.01 Å.

3. DFT-D3 Investigations of Compound I

3.1. Computational Details

The DFT calculations were made based on the crystallographic CIF (Crystallographic Information File) using the DFT/B3LYP-D3/LanL2DZ [28–30] level of theory, as implemented in Gaussian 09 [31]. The represented figures have been selected using Gauss View 5 [32]. Analysis of HOMO and LUMO orbital occupancies gives insights into the electron localization on the surface of the material and the charge transfer mechanisms within the complex [33]. The molecular electrostatic potential (MEP) was determined to investigate the electrophilic and nucleophilic sites on the compound's surface. The Hirshfeld surface (HS) analyses were deeply studied to elucidate the responsible inter- and intra-molecular interactions that contribute to the stability of the compound.

3.2. Optimized Structure of [K(crypt-222)][Fe^{III}(TpivPP)(CO_3)] (**I**)

Figure 9 depicts a side view of our studied compound. Table 4 presents a compilation of selected experimental and calculated bond lengths and angles within the coordination sphere polyhedral surrounding the iron(III) central ion of complex **I**. The comparison between experimental and theoretical values for this dihaptocarbonato iron(III) complex reveals a high degree of proximity. Specifically, the Fe-Np distances are measured at 2.105 (6) Å experimentally and 2.052 Å theoretically, while the Fe-O(axial ligand) distances are recorded at 2.00(2)/2.047(2) Å experimentally and 1.992/2.001 Å theoretically. This difference between the experimental and theoretical distance values may be due to the fact that the calculated values are obtained assuming a gas phase, while the experimental values were obtained from the X-ray crystal structure (solid state).

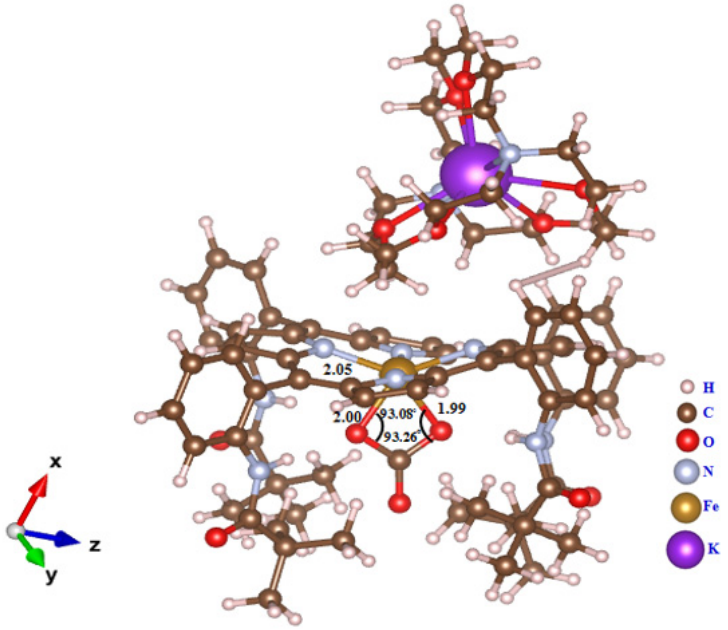


Figure 9. Optimized structure of studied compound **I**.

Table 4. Selected bond lengths (Å) and bond angles (°) of [Fe^{III}(TpivPP(CO_3)]$^-$ (**I**).

Iron Coordination Polyhedron		
	Experimental Values	**Theoretic Values**
Fe-N1	2.115(6)	2.263
Fe-N2	2.083(5)	2.021
Fe-N3	2.120(6)	2.061
Fe-N4	2.101(6)	2.052
Fe-O5A	2.00(2)	1.992
Fe-O6A	2.047(2)	2.001
C65-O5A	1.250(2)	1.367
C65-O6A	1.257(2)	1.365
C65-O7	1.292(1)	1.244
N1-Fe-O5A	110.0(6)	143.44
N1-Fe-O6A	78.3(6)	79.30
N2-Fe-O5A	136.4(6)	143.43
N2-Fe-O6A	90.6(6)	89.90

Table 4. *Cont.*

Iron Coordination Polyhedron		
	Experimental Values	**Theoretic Values**
N3-Fe-O5A	98.3(6)	104.44
N3-Fe-O6A	133.8(6)	142.59
N4-Fe-O5A	76.4(5)	87.67
N4-Fe-O6A	118.4(7)	101.87
N1-Fe-N2	85.9(2)	87.16
N1-Fe-N3	146.7(2)	137.55
N1-Fe-N4	85.0(2)	88.04
N2-Fe-N3	85.4(2)	86.88
N2-Fe-N4	146.9(2)	165.89
Fe-O5A-C65	95.5(1)	93.26
Fe-O6A-C65	91.9(2)	93.08
O5A-C65-O6A	99.1(2)	107.38
O5A-C65-O7	132.8(2)	126.28
O6A-C65-O7	118.6(2)	126.32

Additionally, the Fe-O5A-C65 angle is determined to be approximately 93.26°, closely aligning with the experimental value of 95.50°. It is observed that the H···H interaction is low bonding, formed between the [K(crypt-222)] and the compound. These findings support the notion of strong agreement between theoretical predictions and experimental observations, underscoring the robust stability and effective group interactions within complex **I**.

3.3. HOMO/LUMO and Global Reactivity Investigations

The HOMO and LUMO iso-surfaces are key parameters for determining electron acceptance or donation ability in the compound [34–37]. Molecular orbitals (FMO) provide a clear idea of the electron occupations in the studied material and electronic charge transfer (ECT), aiding in the understanding of the electronic properties of materials [38]. Furthermore, the gap energy gives a clear idea concerning the chemical reactivity, kinetic stability, global hardness-softness characteristics, and optical polarizability of the compound. Moreover, the FMO analysis offers insights into the acceptor regions, which is beneficial for biological applications. The HOMO and LUMO orbitals are shown in Figure 10. Analysis of the HOMO orbital reveals an electron accumulation around the central metal Fe and the anionic axial ligand. Subsequently, these lone pairs of electrons cross the forbidden band to the LUMO orbitals, where they are accumulating along the ligand. This discovery suggests a significant charge transfer occurring between the Fering and the neighboring ligand. The localization of high electron populations on the surface is necessary for biological mechanisms. The $\varepsilon_{HOMO}\varepsilon_{LUMO}$ energies were found to be −5.82 eV and −2.50 eV, respectively. The gap energy was found to be 1.87 eV. This indicates the chemical and kinetic stability of our material, as well as its polarizability properties. Additionally, global reactivity parameters were calculated using Koopman's theorem, with the results presented in Table 5.

A low global hardness value of approximately 0.93 eV was obtained, and it can be concluded that electrons can easily cross from S0 (ground state) to S1 (excited state). The chemical potential (μ) and hardness (η) values are around −3.90 eV and 0.93 eV, as shown in Table 5, suggesting the stability of the compound, a result supported by molecular electrostatic potential (MEP) and FMO analysis. The significant electronegativity (χ = 3.90 eV)

indicates its potential for electronic charge transfer with the target receptor. Furthermore, the high electrophilicity index (ω) of 8.17 eV suggests a highly inhibitory system.

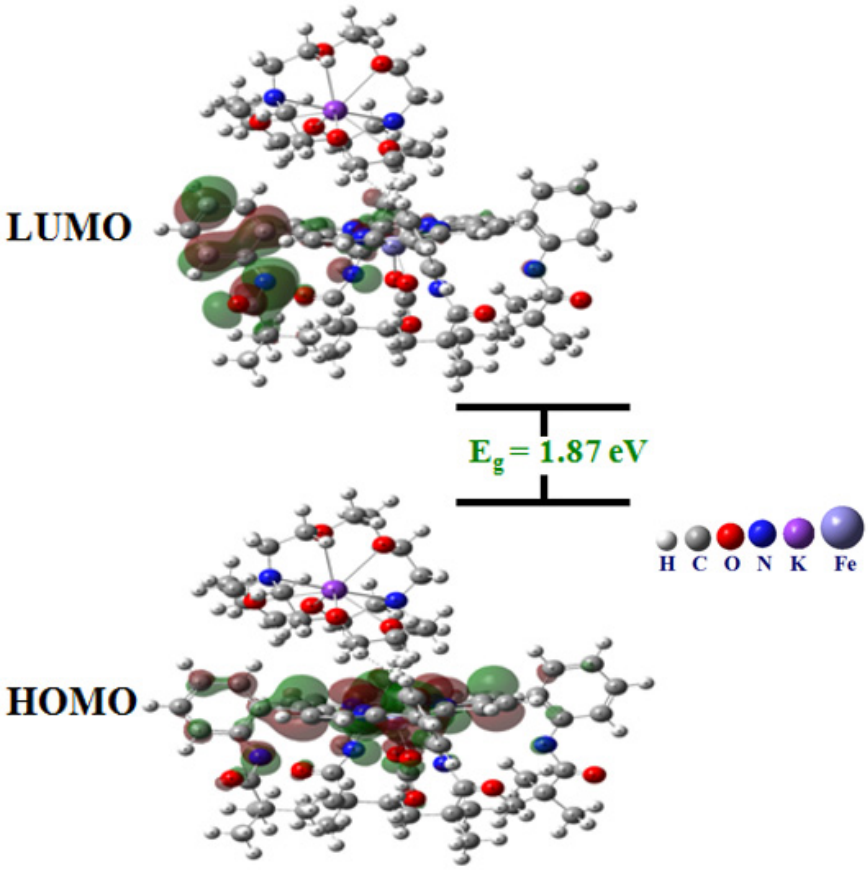


Figure 10. HOMO/LUMO orbital of the current compound.

Table 5. Calculated Quantum chemical parameters for the studied complex.

Quantum Chemical Parameters (eV)	
ε_{HOMO}	−4.84
ε_{LUMO}	−2.97
$E_g = \varepsilon_{LUMO} - \varepsilon_{HOMO}$	1.87
$IP = -\varepsilon_{HOMO}$	4.84
$EA = -\varepsilon_{LUMO}$	2.97
Chemical potential,	−3.90
Mulliken electronegativity, $\chi = -\mu$	3.90
Global hardness, $\eta = \frac{IP-EA}{2}$	0.93
Electrophilicity index, $\omega = \frac{\mu^2}{2\eta}$	8.17

3.4. Molecular Electrostatic Potential (MEP) Analysis

The molecular electrostatic potential (MEP) is a technique that is suitable for determining and understanding the electrophilic (negative potential) and nucleophilic (positive potential) sites that characterize our compound. MEP is an important tool for identifying acceptor and donor attack sites that are useful for sensor and biological applications.

The MEP is represented by color codes identifying the sign of potential in each region, ranging from red to blue. The 3D MEP plot is shown in Figure 11. It can be seen that a dark red color (indicating positive electrostatic potential) surrounds the dihapto-carbonato near the central metal Fe, suggesting a high electronic localization in this area. Additionally, the clear presence of a positive electrostatic potential (blue region) around

the iron and neighboring groups indicates the electrophilic nature of this area. This finding concluded that a highly electronic/energy charge transfer takes place on the surface of the studied compound, as confirmed by FMO analyses. The identification of the existence of double electrophilic and nucleophilic sites resulted in the exceptional ability of [K(2,2,2-crypt)][Fe^{III}(TpivPP)(CO_3)] to function as both electron donors and acceptors. This highlights the high capacity of this material for potential applications in sensors and biological applications.

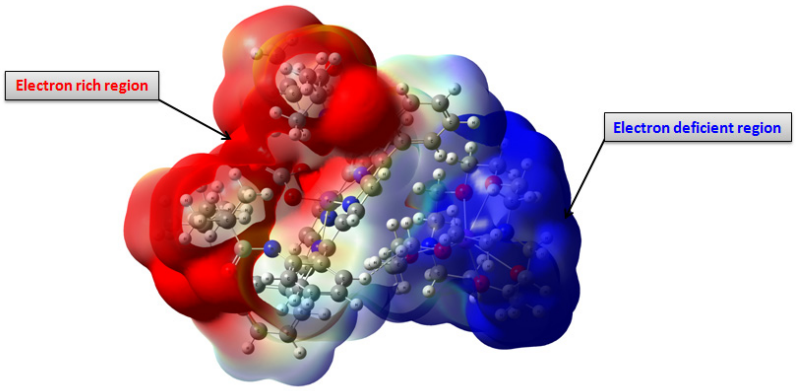


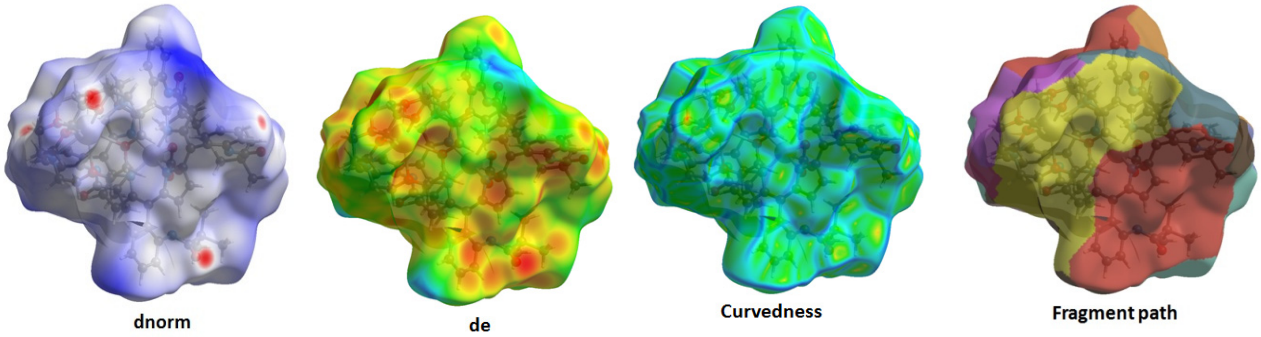
Figure 11. MEP plot of studied compound **I**.

3.5. Hirshfeld Surface (HS) Analysis

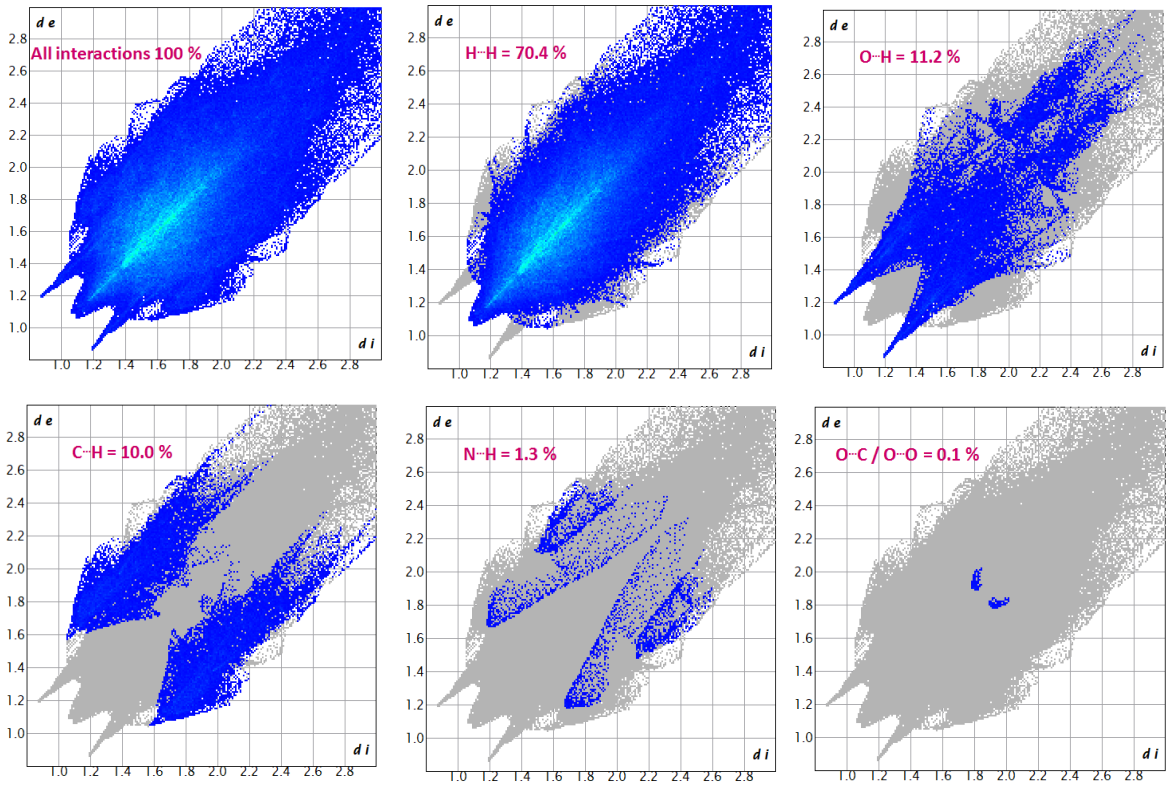
Hirshfeld surface (HS) and two-dimensional (2D) fingerprint plots are robust analytical tools that provide a comprehensive insight into intra- and intermolecular interactions within the crystal lattice [39,40]. The HS serves as a valuable resource for comprehending the co-existing forces between constituent groups within the crystal structure, which ultimately dictate the stability of the molecular complex [41]. The 2Dfingerprint plot is generated as a d_e in the function of d_i, representing the percentage of atomic contacts. The HS iso-surfaces offer a visual representation of interaction through a color-coded scheme, with red, white, and blue spots denoting varying degrees of interaction intensity. Dark red regions signify strong hydrogen bonding interactions; white regions indicate proximity in van der Waals contacts; and blue regions represent longer-range interactions. The $d_{norm}$is located between −0.4481 Å and −0.8821 Å, the shape index is −1 to 1 Å, and the curvedness varies from −4 to 0.4 Å. The normalized distance d_{norm} is calculated using the following formula [42,43]:

$$d_{norm} = \frac{d_i - r_i^{vdw}}{r_i^{vdw}} + \frac{d_e - r_e^{vdw}}{r_e^{vdw}}$$

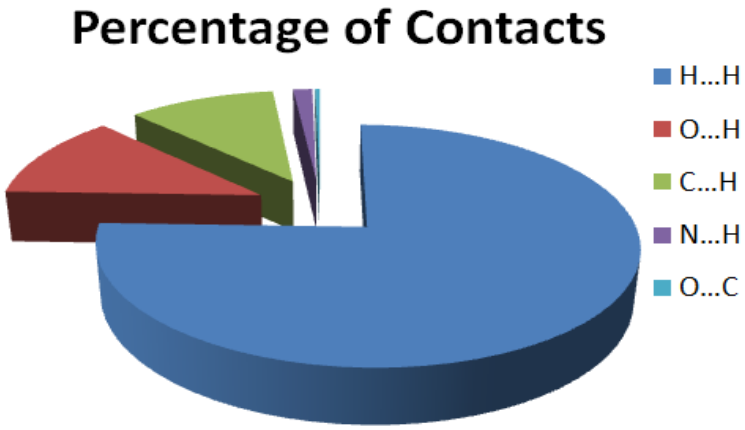
The d_{norm} is intricately linked to both d_e and d_i, where the parameters r_i^{vdw} and r_e^{vdw} delineate the van der Waals radii of the atom. The d_{norm}, d_e, curvedness, fragment path, and 2Dfingerprint plot have been illustrated in Figure 12a,b. The percentages of contacts have been graphically represented in a 2D diagram, as depicted in Figure 12c. H···H interactions dominate the Hirshfeld surface, accounting for 77.4% of the total surface area. The next significant contributions are C···H and O···H interactions in the crystal packing, making up 10.0% and 11.2%, respectively, as depicted in the 2Dfingerprint plot. This finding suggests that these interactions may be enhanced by the electron delocalization on [K(2,2,2-crypt)][Fe^{III}(TpivPP)(CO_3)] surfaces. Interatomic contacts involving N···H, O···C, and O···O exhibit lower contributions in the crystal structure, with percentages of 1.3% and 0.1%, respectively. Analysis of the HS and 2Dfingerprint plots revealed that the robust stability of the functional groups within our compound may provide excellent electronic properties for our novel system.



(**a**)



(**b**)



(**c**)

Figure 12. (**a**) d_{norm}, d_e, shape index, and curvedness; (**b**) the 2Dfingerprint plot; and (**c**) the 2Ddiagram of the percentage of contacts in the current complex **I**.

4. Conclusions

Complex **I** was synthesized and characterized by UV-vis and FT-IR spectroscopic methods. The high-spin of complex **I** is confirmed by the equatorial mean distance of 2.105(6) Å between Fe(III) and the nitrogen atoms of the pyrrole rings. These studies validate that six-coordinated high-spin iron(III) porphyrinates, such as $[Fe(Porph)(X)]^{-}$(X corresponds to the bidentate anionic ligand), exhibit this characteristic. Additionally, the N atoms of the four pyrrole rings, the α-carbon positions of these pyrroles, and the O atoms of the carbonate (CO_3^{2-}) axial ligand contribute to the overall reactivity of this high-spin (S = 5/2) ferric metalloporphyrin, indicating its highly reactive and electron-accepting nature. Molecular electrostatic potential (MEP) calculations provide insight into the electrophilic/nucleophilic properties of complex **I**, while frontier molecular orbital (FMO) analyses reveal significant electronic charge transfer around the central Fe(III) ion. The MEP analysis further confirms the significant electron-accepting behavior of this novel ferric porphyrinic compound. The HS analyses confirm the atomic reorganization and stability of our compound through hydrogen bonding interactions with its neighboring unit cell in the crystal packing.

Supplementary Materials: The following supporting information can be downloaded at: https://www.mdpi.com/article/10.3390/molecules29163722/s1, The synthesis of picket fence porphyrin (H_2TpivPP), UV/Vis spectroscopy, and X-ray molecular structure of the $[K(2,2,2\text{-crypt})]^{+}$ counter-ion are reported in Scheme S1 and Figures S1 and S2. Table S1. Electronic absorption data for complex I and a selection of meso-arylporphyrin compounds. Refs. [44–52] are cited in Supplementary Materials.

Author Contributions: M.D., B.G., M.A.L., A.S.K. (Anna S. Kazachenko) and A.S.K. (Aleksandr S. Kazachenko): conceptualization, methodology, writing—original draft, writing, review and editing. O.M.A.-D. and N.I.: review and editing, H.N.: conceptualization, validation, supervision, methodology, and review of the manuscript. All authors have read and agreed to the published version of the manuscript.

Funding: This research received no external funding.

Institutional Review Board Statement: Not applicable.

Data Availability Statement: CCDC 2367771 contains the supplementary crystallographic data for this paper. These data can be obtained free of charge via https://www.ccdc.cam.ac.uk/structures/search?Ccdc=2367771&Author=dhifet&Access=referee (accessed on 16 July 2024), or from the Cambridge Crystallographic Data Center, 12 Union Road, Cambridge CB2 1EZ, UK; fax: (+44)-1223-336-033; or e-mail: deposit@ccdc.cam.ac.uk.

Acknowledgments: This study was supported by the Researchers Supporting Project No. RSP2024R61 of King Saud University, Riyadh, Saudi Arabia.

Conflicts of Interest: The authors declare that they have no financial interests or personal relationships that could influence the work described in this paper.

References

1. Scheidt, W.R.; Hoard, J.L. Hoard, Stereochemistry of low-spin cobalt porphyrins. I. Structure and bonding in a nitrosylcobalt porphyrin and their bearing on one rational model for the oxygenated. *J. Am. Chem. Soc.* **1973**, *95*, 8281–8288. [CrossRef] [PubMed]
2. La Mar, G.N.; Walker, F.A. Dynamics of axial ligation in metalloporphyrins. I. Imidazole exchange in low-spin ferric porphyrins. *J. Am. Chem. Soc.* **1972**, *94*, 8607–8608. [CrossRef] [PubMed]
3. Collman, J.P.; Gagne, R.R.; Halbert, T.R.; Marchon, J.C.; Reed, C.A. Reversible oxygen adduct formation in ferrous complexes derived from a picket fence porphyrin. Model for oxymyoglobin. *J. Am. Chem. Soc.* **1973**, *95*, 7868–7870. [CrossRef] [PubMed]
4. Hoffman, B.M.; Ratner, M.A. Gated electron transfer: When are observed rates controlled by conformational interconversion? *J. Am. Chem. Soc.* **1980**, *109*, 6237–6243. [CrossRef]
5. Patra, R.; Chaudhary, A.; Ghosh, S.K.; Rath, S.P. Modulation of Metal Displacements in a Saddle Distorted Macrocycle: Synthesis, Structure, and Properties of High-Spin Fe(III) Porphyrins and Implications for the Hemoproteins. *Inorg. Chem.* **2008**, *47*, 8324–8335. [CrossRef] [PubMed]
6. Walker, F.A. Models of the bis-histidine-ligated electron-transferring cytochromes. Comparative geometric and electronic structure of low-spin ferro-and ferrihemes. *Chem. Rev.* **2004**, *104*, 589–616. [CrossRef] [PubMed]

7. Montiel-Montoya, R.; Bill, E.; Gonser, U.; Lauer, S.; Trautwein, A.X.; Schappacher, M.; Ricard, L.; Weiss, R. Mössbauer Studies of Synthetic Analogues for the Active Site in Cytochromes P450. In *The Coordination Chemistry of Metalloenzymes: The Role of Metals in Reactions Involving Water, Dioxygen and Related Species. Proceedings of the NATO Advanced Study Institute held at San Miniato, Pisa, Italy, 28 May–8 June 1982*; Springer: Dordrecht, The Netherlands, 1983.
8. Hirshfeld, F.L. Bonded-atom fragments for describing molecular charge densities. *Theor. Chim. Acta* **1977**, *44*, 129–138. [CrossRef]
9. Wolff, S.K.; Grimwood, D.J.; McKinnon, J.J.; Turner, M.J.; Jayatilaka, D.; Spackman, M.A. CrystalExplorer: A program for Hirshfeld surface analysis, visualization and qu antitative analysis of molecular crystals. *J. Appl. Cryst.* **2013**, *54*, 1006–1011. [CrossRef]
10. Spackman, M.A.; Jayatilaka, D. Hirshfeld surface analysis. *Cryst. Eng. Commun.* **2009**, *11*, 19–32. [CrossRef]
11. Spackman, M.A.; McKinnon, J.J. Fingerprinting intermolecular interactions in molecular crystals. *Cryst. Eng. Commun.* **2002**, *4*, 378–392. [CrossRef]
12. Collman, J.P.; Gagne, R.R.; Reed, C.; Halbert, T.R.; Lang, G.; Robinson, W.T. Robinsonlc, Picket fence porphyrins. Synthetic models for oxygen binding hemoproteins. *J. Am. Chem. Soc.* **1975**, *97*, 1427–1439. [CrossRef] [PubMed]
13. Bruker, A. *Instrument Service v4. 2.7, APEX2, SADABS, SAINT-Plus & XPREP*; Bruker AXS Inc.: Madison, WI, USA, 2014.
14. Burla, M.C.; Caliandro, R.; Carrozzini, B.; Cascarano, G.L.; Cuocci, C.; Giacovazzo, C.; Mallamo, M.; Mazzone, A.; Polidori, G. Crystal structure determination and refinement via SIR2014. *J. Appl. Cryst.* **2005**, *48*, 306–309. [CrossRef]
15. Sheldrick, G.M. SHELXT–Integrated space-group and crystal-structure determination. *Acta Cryst.* **2014**, *71*, 3–8. [CrossRef] [PubMed]
16. Mcardle, P. SORTX—A program for on-screen stick-model editing and autosorting of SHELX files for use on a PC. *J. Appl. Cryst.* **1995**, *28*, 65. [CrossRef]
17. Spek, A.L. Structure validation in chemical crystallography. *Acta. Cryst.* **2009**, *65*, 148–155. [CrossRef] [PubMed]
18. Farrugia, L.J. ORTEP-3 for Windows-a version of ORTEP-III with a Graphical User Interface (GUI). *J. Appl. Cryst.* **1997**, *30*, 565. [CrossRef]
19. Macrae, C.F.; Bruno, I.J.; Chisholm, J.A.; Edgington, P.R.; McCabe, P.; Pidcock, E.; Rodriguez-Monge, L.; Taylor, R.; van de Streek, J.; Wood, P.A. Mercury CSD 2.0–new features for the visualization and investigation of crystal structures. *J. Appl. Crystallogr.* **2008**, *41*, 466–470. [CrossRef]
20. Spek, A.L. PLATON SQUEEZE: A tool for the calculation of the disordered solvent contribution to the calculated structure factors. *Acta Crystallogr.* **2015**, *71*, 9–18. [CrossRef]
21. Allen, F.H.; Kennard, O.; Watson, D.G.; Brammer, L.; Orpen, A.G.; Taylor, R. Tables of bond lengths determined by X-ray and neutron diffraction. Part 1. Bond lengths in organic compounds. *J. Chem. Soc. Perkin Trans.* **1987**, *2*, S1–S19. [CrossRef]
22. Dhifet, M.; Belkhiria, M.S.; Giorgi, M.; Nasri, H. Preparation, UV–Vis, IR and ^{1}H NMR spectra, and molecular structure of the complex ion (η^2-carbonato)(α,α,α,α-tetrakis (o-pivalamidophenyl) porphinato) ferrate (III). *Inorg.Chim. Acta* **2009**, *362*, 2776–2781. [CrossRef]
23. Phillippi, M.A.; Baenziger, N.; Goff, H.M. Preparation, solution properties, and structure of iron (III) porphyrin oxyanion complexes. Crystal and molecular stereochemistry of a novel bidentate nitrato complex. *Inorg. Chem.* **1981**, *23*, 3904–3911. [CrossRef]
24. Kellett, P.J.; Pawlik, M.J.; Taylor, L.F.; Thompson, R.G.; Levstik, M.A.; Anderson, O.P.; Strauss, S.H. Five-and six-coordinate high-spin iron (III) porphyrin complexes with teflate ($OTeF^{5-}$) ligands. *Inorg. Chem.* **1989**, *28*, 440–447. [CrossRef]
25. Nasri, H.; Haller, K.J.; Wang, Y.; Hanh, H.B.; Scheidt, W.R. Reactions of bis (nitro)[.alpha.,.alpha.,.alpha.,.alpha.-meso-tetrakis(o-pivalamidophenyl)porphinato]iron(III) with 2,3,5,6-tetrafluorothiophenol and 2,3,5,6-tetrafluorothiophenolate. EPR and Moessbauer spectra and molecular structures. *Inorg. Chem.* **1992**, *31*, 3459–3467. [CrossRef]
26. Doppelt, P.; Fischer, J.; Weiss, R. Synthesis and Structure of a Dimercapto—Iron(III) Porphyrin Derivative: [Fe(SC6HF4)2TPP] [Na c 18C6], C6H6. *Croat. Chem. Acta* **1984**, *57*, 507–518.
27. Scheidt, W.R.; Lee, Y. Recent advances in the stereochemistry of metallotetrapyrroles. *Struct. Bond.* **1987**, *64*, 1–70.
28. Grimme, S. Semi empirical hybrid density functional with perturbative second order correlation. *J. Chem. Phys.* **2006**, *124*, 034108. [CrossRef]
29. Lee, C.; Yang, W.; Parr, R.G. Development of the Colle-Salvetti correlation-energy formula into a functional of the electron density. *Phys. Rev. B* **1988**, *37*, 785–789. [CrossRef] [PubMed]
30. Hay, P.J.; Wadt, W.R. Ab initio effective core potentials for molecular calculations. Potentials for the transition metal atoms Sc to Hg. *J. Chem. Phys.* **1985**, *82*, 270–283. [CrossRef]
31. G09 | Gaussian.com. Available online: https://gaussian.com/glossary/g09/ (accessed on 10 June 2024).
32. Roy, D.D.; Todd, A.K.; John, M.M. *Gauss View, 5.0. 8*; Gaussian Inc.: Wallingford, UK; Wallingford, CT, USA, 2009.
33. Choudhary, V.; Bhatt, A.; Dash, D.; Sharma, N. DFT calculations on molecular structures, HOMO–LUMO study, reactivity descriptors and spectral analyses of newly synthesized diorganotin(IV) 2-chloridophenylacetohydroxamate complexes. *J. Comput. Chem.* **2019**, *40*, 2354–2363. [CrossRef] [PubMed]
34. Fasiuddin, G.; Basha, A.A.; Kubaib, A.; Azam, M.; Muzammil, P.; Bouzid, G.; Ayachi, S.; Khan, F.L.A.; Imran, P.M.; Al-Resayes, S.I. Solvation model, Vibrational analysis, Electronic level, Non-Covalent interactions and Molecular docking investigations of 6-Chloro-2-(4-Aminophenyl)-1H-Benzimidazole. *J. Mol. Liq.* **2024**, *398*, 124315. [CrossRef]

35. Guillén-López, A.; Cabrera, O.G.R.; de la Cruz Arreola, S.; Celaya, C.A.; Sevilla-Camacho, P.Y.; Muñiz, J. Exploring the potential of porphyrin-based materials for organic solar cells supported on carbon: A quantum chemistry approach. *J. Photochem. Photobiol. A Chem.* **2024**, *449*, 115401. [CrossRef]
36. Jumabaev, A.; Holikulov, U.; Hushvaktov, H.; Issaoui, N.; Absanov, A. Intermolecular interactions in ethanol solution of OABA: Raman, FTIR, DFT, M062X, MEP, NBO, FMO, AIM, NCI, RDG analysis. *J. Mol. Liq.* **2023**, *377*, 121552. [CrossRef]
37. Hijazi, S.; Ahmed, N.; Louis, H.; Anna, I.; Shah, W.A. Biological and computational studies of novel scaffolds of gallic acid: Insight from density functional theory and molecular docking studies. *Anal. Chem. Lett.* **2023**, *13*, 487–504. [CrossRef]
38. Owen, A.E.; Anyambula, I.A.; Benson, C.U.; Ojumola, F.O.; Alawa, J.A.; Benjamin, I.; Iyam, S.O.; Ogar, C.U.; Ojong, M.A.; Ojong, R.; et al. Exploration of semi-carbazone derivatives as promising agents against cholera: Insights from spectroscopic analysis, reactivity studies (ELF, HOMO-LUMO, NBO), solvation effects, and molecular docking investigations. *Chem. Phys. Impact* **2024**, *8*, 100438. [CrossRef]
39. Riaz, M.; Ali, A.; Ashfaq, M.; Ibrahim, M.; Akram, N.; Tahir, M.N.; Kuznetsov, A.; Rodríguez, L.; Sameeh, M.Y.; Assiri, M.A.; et al. Polymorphs of Substituted p-Toluenesulfonanilide: Synthesis, Single-Crystal Analysis, Hirshfeld Surface Exploration, and Theoretical Investigation. *ACS Omega* **2023**, *8*, 35307–35320. [CrossRef] [PubMed]
40. Siddiqui, S.W.A.; Ashraf, A.; Ashfaq, M.; Tahir, M.N.; Niaz, S. Sulfonamide derived Schiff base Mn (II), Co (II), and Ni (II) complexes: Crystal structures, density functional theory and Hirshfeld surface analysis. *Appl. Organomet. Chem.* **2023**, *37*, 7077. [CrossRef]
41. Fatima, A.; Kumar, A.; Saral, A.K.A.; Muthu, S.; Afzal, M.; Haq, N.; Nazar, I.; Siddiqui, N.; Javed, S. Study of L-tryptophan (a neurotransmitter precursor): Spectral, Hirshfeld surface, molecular docking and dynamics simulations. *Z. Phys. Chem.* **2023**. [CrossRef]
42. Mackenzie, C.F.; Spackman, P.R.; Jayatilaka, D.; Spackman, M.A. CrystalExplorer model energies and energy frameworks: Extension to metal coordination compounds, organic salts, solvates and open-shell systems. *IUCrJ* **2017**, *4*, 575–587. [CrossRef] [PubMed]
43. McKinnon, J.J.; Jayatilaka, D.; Spackman, M.A. Towards quantitative analysis of intermolecular interactions with Hirshfeld surfaces. *Chem. Commun.* **2007**, 3814–3816. [CrossRef]
44. Ezzayani, K.; Khelifa, A.B.; Saint-Aman, E.; Loiseau, F.; Nasri, H. Synthesis, spectroscopic characterizations, cyclic voltammetry investigation and molecular structure of the di-μ-cyanato-*N*-bis(μ-1,4,7,10,13,16-hexaoxacyclooctadecane)bis(5,10,15,20-tetraphenylporphyrinato) dimagnesiumdipotassium complex. *Polyhedron* **2016**, *117*, 817. [CrossRef]
45. Amiri, N.; Taheur, F.B.; Chevreux, S.; Wenger, E.; Lemercier, G.; Nasri, H. Synthesis, crystal structure and spectroscopic characterizations of porphyrin-based Mg (II) complexes–Potential application as antibacterial agent. *Tetrahedron* **2017**, *73*, 7011. [CrossRef]
46. Amiri, N.; Hajji, M.; Taheur, F.B.; Chevreux, S.; Roisnel, T.; Lemercier, G.; Nasri, H. Two novel magnesium (II) meso-tetraphenylporphyrin-based coordination complexes: Syntheses, combined experimental and theoretical structures elucidation, spectroscopy, photophysical properties and antibacterial activity. *J. Solid State Chem.* **2018**, *258*, 477. [CrossRef]
47. Fradi, T.; Noureddine, O.; Taheur, F.B.; Guergueb, M.; Nasri, S.; Amiri, N.; Almahri, A.; Roisnel, T.; Guerineau, V.; Issoui, N.; et al. New DMAP meso-arylporphyrin Magnesium(II) complex. Spectroscopic, Cyclic voltammetry and X-ray molecular structure characterization. DFT, DOS and MEP calculations and Antioxidant and Antifungal activities. *J. Mol. Struct.* **2021**, *1236*, 130299. [CrossRef]
48. Bominaar, E.L.; Ding, X.Q.; Gismelseed, A.; Bill, E.; Winkler, H.; Trautwein, A.X.; Nasri, H.; Fischer, J.; Weiss, R. Weiss, Structural, Moessbauer, and EPR investigations on two oxidation states of a five-coordinate, high-spin synthetic heme. Quantitative interpretation of zero-field parameters and large quadrupole splitting. *Inorg. Chem.* **1992**, *31*, 1845. [CrossRef]
49. Nasri, H.; Debbabi, M. Synthesis, spectroscopic and structural characterization of the pentacoordinate high-spin Fe (III) isothiocyanate "picket fence" porphyrin complex. *Polyhedron* **1998**, *17*, 3607. [CrossRef]
50. Belkhiria, M.S.; Dhifet, M.; Nasri, H. Preparation and spectroscopic properties of the (cyanato-N) and (oxalato) iron(III) "picket fence" porphyrins: Structure of the (cyanato-N)(α,α,α,α-tetrakis(o-pivalamidophenyl)porphinato)iron(III) complex. *J. Porphyr. Phthalocyanines* **2005**, *9*, 575. [CrossRef]
51. Nasri, H.; Goodwin, J.A.; Scheidt, W.R. Use of protected binding sites for nitrite binding in iron(III) porphyrinates. Crystal structure of the bis(nitro)(.alpha.,.alpha.,.alpha.,.alpha.-tetrakis(o-pivalamidophenyl)porphinato)iron(III) anion. *Inorg. Chem.* **1990**, *28*, 185. [CrossRef]
52. Nasri, H.; Wang, Y.; Huynh, B.H.; Walker, F.A.; Scheidt, W.R. Reactions of bis(nitro)(.alpha.,.alpha.,.alpha.,.alpha.-tetrakis(o-pivalamidophenyl)porphinato)ferrate(III) with pyridine and imidazole. EPR and Moessbauer spectra and molecular structures of the mixed-ligand species. *Inorg. Chem.* **1991**, *30*, 1483. [CrossRef]

Disclaimer/Publisher's Note: The statements, opinions and data contained in all publications are solely those of the individual author(s) and contributor(s) and not of MDPI and/or the editor(s). MDPI and/or the editor(s) disclaim responsibility for any injury to people or property resulting from any ideas, methods, instructions or products referred to in the content.